Commun. Comput. Phys.
doi: 10.4208/cicp.260313.291113a

Vol. **16**, No. 1, pp. 136-168
July 2014

Numerical Study of Stability and Accuracy of the Immersed Boundary Method Coupled to the Lattice Boltzmann BGK Model

Yongguang Cheng[1,*], Luoding Zhu[2] and Chunze Zhang[1]

[1] *State Key Laboratory of Water Resources and Hydropower Engineering Science, Wuhan University, Wuhan 430072, P.R. China.*
[2] *Department of Mathematical Sciences, Indiana University-Purdue University Indianapolis, Indianapolis, IN 46202, USA.*

Received 26 March 2013; Accepted (in revised version) 29 November 2013

Communicated by Ming-Chih Lai

Available online 10 April 2014

Abstract. This paper aims to study the numerical features of a coupling scheme between the immersed boundary (IB) method and the lattice Boltzmann BGK (LBGK) model by four typical test problems: the relaxation of a circular membrane, the shearing flow induced by a moving fiber in the middle of a channel, the shearing flow near a non-slip rigid wall, and the circular Couette flow between two inversely rotating cylinders. The accuracy and robustness of the IB-LBGK coupling scheme, the performances of different discrete Dirac delta functions, the effect of iteration on the coupling scheme, the importance of the external forcing term treatment, the sensitivity of the coupling scheme to flow and boundary parameters, the velocity slip near non-slip rigid wall, and the origination of numerical instabilities are investigated in detail via the four test cases. It is found that the iteration in the coupling cycle can effectively improve stability, the introduction of a second-order forcing term in LBGK model is crucial, the discrete fiber segment length and the orientation of the fiber boundary obviously affect accuracy and stability, and the emergence of both temporal and spatial fluctuations of boundary parameters seems to be the indication of numerical instability. These elaborate results shed light on the nature of the coupling scheme and may benefit those who wish to use or improve the method.

AMS subject classifications: 76M28, 74F10

Key words: Immersed boundary method, lattice Boltzmann method, fluid-structure interaction, flexible boundary, complex boundary, accuracy, stability, verification.

*Corresponding author. *Email addresses:* ygcheng@whu.edu.cn (Y. G. Cheng), lzhu@math.iupui.edu (L. Zhu)

1 Introduction

The immersed boundary (IB) method is both a novel mathematical formulation and a numerical method for fluid-structure interaction (FSI). It is particularly suitable for FSI problems with flexible structures, while rigid boundaries can also be treated well. The first version of the IB method was proposed by C. Peskin [1] in 1972 for simulating the flow patterns around natural heart valves. It has become a general method for computer simulation of biological structures interacting with fluids [2]. Some representative applications of IB methods include: blood flow in the human heart [3, 4], FSI of natural and prosthetic cardiac valves [5, 6], aquatic animal locomotion [7], wave propagation in the cochlea [8], platelet aggregation during blood clotting [9], flow of suspensions [10], valveless pumping [11], flow and transport in renal arterioles [12], cell and tissue deformation under shear flow [13], insect flight [14], hemodynamics in the aorta [15], free swimmers in viscoelastic fluids [16], diffusion of integral membrane proteins [17], and dynamics of parachute opening [18].

Since Peskin's pioneering work, many modifications and refinements have been proposed to extend and improve the method. These include the immersed interface method which was an improvement to second-order accuracy for a neutrally-buoyant closed boundary [19], the blob-projection method which was an improvement to higher Reynolds numbers [20], the immersed continuum method which was extension to finite element formulation [21], and the immersed finite element method which was an extension to the compressible case using a finite element formulation [22]. Within the IB method itself, there exist quite a few different versions. These include the original versions [2],the volume conserved version [23], the adaptive mesh refinement version [24], the (formally) second-order versions [25, 45], the multigrid version [26], the penalty version [27], the implicit versions [28], and the lattice-Boltzmann (LB) version [29–35].

The lattice Boltzmann version of IB method has been undergoing a rapid development in recent years, partly because the LB method [52] is an efficient, relatively simple, and essentially parallel scheme for fluid flow simulations, and the IB-LB coupling has been proven to be effective for simulating fluid-structure interaction (FSI). Some works along this line include [29–39]. Feng et al. first published a coupled IB-LB scheme for simulating particle-fluid interaction problems [34]. Later, Peng upgraded the scheme by using a multi-block lattice and multi-relaxation-time LB scheme to enhance stability and to implement local grid refinement [35]. Shu improved the convergence of the coupling scheme by correcting the velocity to enforce the physical boundary conditions [37]. Dupuis simulated the flow past an impulsively started cylinder [38]. Niu improved the calculation of the boundary force on the fluid [39]. Peng carried out comparative study of IB-LB and LB bounce-back treatment of boundary [36]. Kang compared direct-forcing IB-LB methods for stationary complex boundaries [44]. The above works were intended for *rigid*-body-fluid interaction. On the other hand, for FSI problems with *flexible* boundary, Cheng proposed a scheme suitable for rapidly moving boundary and large pressure gradient [43], Hao proposed an implicit scheme to improve the robustness [41], Zhang

simulated red blood cell aggregation [30,31], Cheng simulated the mitral valve flow [29], Zhu simulated a flexible sheet interacting with a 3D flow [32], Tian simulated the flapping of multiple elastic filaments [42], and Krueger [33] analyzed the efficiency and accuracy of simulating multiple deformable particles by an IB-LB finite element method. It should be pointed out that the IB method used in all of the above works is based on Peskin's ideas, and the IB-LB coupling methods for rigid boundaries are just the special case of those for flexible boundaries.

The accuracy and robustness are the most important issues for the IB methods. Inaccuracy at immersed boundary not only reduces the speed of convergence but also gives spurious results on some occasions. Volume leakage was a problem in simulating closed membranes [23, 47], boundary slip was observed at the non-slip boundary [36, 46], and velocity profiles near boundary were found abnormal [46]. Instability always causes the abortion of simulations in practice for problems of large boundary stiffness. When simulating rapidly moving boundaries, explicit schemes may blow up at the very early stage of a simulation [48]. Accuracy and stability are interlaced and are all related to the coupling scheme between the fluid flow solver and the structural boundary solver. The IB-LB coupling schemes also suffer from these problems [35–37, 43, 46]. Because most of the existing works use the popular Bhatnagar-Gross-Krook (BGK) collision operator in the coupling scheme (IB-LBGK coupling), the accuracy and stability issues need careful studies in this setting. However, the study of accuracy and stability of IB-LBGK coupling scheme is so far insufficient. The accuracy at the immersed boundary, from the application point of view, may be classified as volume conservation of a closed boundary, boundary velocity consistency (the flow velocity at the boundary may deviate from the velocity of the boundary itself), near boundary velocity profile (the velocity profile within the FSI bandwidth may be abnormal), and pressure maintenance (the preservation of steep pressure difference across a closed boundary). Extensive studies on these numerical issues and their intrinsic mechanisms are necessary and important.

This paper aims to study the numerical features of the new IB-LBGK coupling scheme proposed in [43] by four specific cases–the relaxation of a circular membrane, the shearing flow induced by a moving fiber in the middle of a channel, the shearing flow near the non-slip wall, and the laminar circular Couette flow between two inversely rotating cylinders. They are used to verify the accuracy and robustness, and provide some insights for applications and future improvements of the scheme. In Section 2, the ideas, procedures and different coupling functions of the IB-LBGK coupling scheme are introduced. In Section 3, the four test problems are described. Analysis and discussion of several aspects related to accuracy and robustness are addressed in Section 4. At the end of the paper a conclusion is given.

2 The IB-LBGK coupling scheme

2.1 The IB method for flexible immersed boundaries

2.1.1 Formulation of the IB method

In the IB method, an Eulerian description of the Navier-Stokes (N-S) equations is used for the fluid dynamics, and a Lagrangian description of a curvilinear boundary (e.g., a fiber) is used for structural mechanics of objects immersed in the fluid. The formulation may be expressed as follows [43, 53]:

$$\frac{\partial \rho}{\partial t}+\nabla\cdot(\rho \boldsymbol{u})=0, \tag{2.1}$$

$$\frac{\partial(\rho \boldsymbol{u})}{\partial t}+\nabla\cdot(\rho \boldsymbol{u}\boldsymbol{u})=-\nabla p+\nu\nabla\cdot[\rho(\nabla \boldsymbol{u}+(\nabla \boldsymbol{u})^T)]+\boldsymbol{f}, \tag{2.2}$$

$$\frac{\mathrm{d}\boldsymbol{X}(s,t)}{\mathrm{d}t}=\boldsymbol{U}(\boldsymbol{X}(s,t),t)=\int_{\Omega_f}\boldsymbol{u}(\boldsymbol{x},t)\delta(\boldsymbol{x}-\boldsymbol{X}(s,t))\mathrm{d}\boldsymbol{x}, \tag{2.3}$$

$$\boldsymbol{f}(\boldsymbol{x},t)=\int_{\Gamma_b}\boldsymbol{F}(s,t)\delta(\boldsymbol{x}-\boldsymbol{X}(s,t))\mathrm{d}s, \tag{2.4}$$

$$\boldsymbol{F}(s,t)=\mathcal{S}_f\boldsymbol{X}(s,t), \tag{2.5}$$

where $\boldsymbol{X}$, $\boldsymbol{F}$ and $\boldsymbol{U}$ are the Lagrangian boundary position, boundary force density and boundary moving speed, respectively; $\boldsymbol{x}$, $\boldsymbol{f}$, $\boldsymbol{u}$, p, ρ and ν are the Eulerian spatial coordinate, external force density, flow velocity, flow pressure, fluid density and kinematic viscosity, respectively; s is the Lagrangian coordinates of the boundary, $\mathcal{S}_f$ is the boundary force generating operator, and $\delta(\boldsymbol{r})$ is the Dirac delta function. Eqs. (2.1) and (2.2) are the N-S equations with external force $\boldsymbol{f}$ in Eulerian form for the fluid flow domain Ω_f, while Eqs. (2.3) and (2.5) are the immersed boundary equations in Lagrangian form for the boundary Γ_b. The left part of Eq. (2.3) describes the boundary kinematics. Eq. (2.5) denotes the operator computing the force $\boldsymbol{F}$ from the configuration of the immersed boundary with the operator $\mathcal{S}_f$ being problem-dependent. Eq. (2.4) and the right part of Eq. (2.3) are the interaction equations of fluid and boundary. The former converts the Lagrangian force to the Eulerian force and the latter imposes the flow velocity on the boundary to obtain the boundary speed $\boldsymbol{U}$. The interaction is realized by using the coupling kernel, i.e., an integral on the Dirac delta function $\delta(\boldsymbol{r})$.

2.1.2 Boundary force calculation

The boundary force $\boldsymbol{F}$ is computed from the fiber configuration. For a fiber with tensive, bending, and fastening forces, Eq. (2.5) can be expressed in practice as

$$\boldsymbol{F}=k_s\frac{\partial^2\boldsymbol{X}}{\partial s^2}-k_b\frac{\partial^4\boldsymbol{X}}{\partial s^4}-k_f(\boldsymbol{X}-\boldsymbol{Z}), \tag{2.6}$$

in which k_s is the fiber tension stiffness, k_b the fiber bending rigidity, k_f the fastening stiffness, and $\boldsymbol{Z}$ the fastening or target position of the fiber. If the movement of boundary is given, then $\boldsymbol{Z}$ can be the prescribed boundary position (target position). For rigid boundary problems, $\boldsymbol{Z}$ is the position of boundary.

When discretized along the fiber arc length, Eq. (2.6) may be expressed in the finite difference form:

$$\begin{aligned}\boldsymbol{F}_k=&k_s\left(\frac{\boldsymbol{X}_{k-1}-2\boldsymbol{X}_k+\boldsymbol{X}_{k+1}}{\Delta s^2}\right)-k_b\left(\frac{\boldsymbol{X}_{k-2}-4\boldsymbol{X}_{k-1}+6\boldsymbol{X}_k-4\boldsymbol{X}_{k+1}+\boldsymbol{X}_{k+2}}{\Delta s^4}\right)\\&-k_f(\boldsymbol{X}_k-\boldsymbol{Z}_k).\end{aligned}\tag{2.7}$$

Note that this formula is based on a uniform Lagrangian grid. Should a non-uniform grid has to be used (though very rare in practice) a corresponding finite difference scheme should be adopted. Formula (2.7) is for both flexible and rigid boundaries. The rigid boundary is actually a special case of the flexible boundary. When large fastening and stiffness coefficients are given, one may use the same formula to simulate problems with rigid boundaries. After the forces $\boldsymbol{F}_k$ $(k=0,1,\cdots,n_b)$ at fiber points are known, one can use Eq. (2.8) to calculate the Eulerian forces the boundary exerts on the fluid. Then, it is the task of the LB method to solve the N-S equations with an external forcing term.

2.1.3 Discrete form of the interaction equations

The above equations are solved on a pair of computational grids: a cell-centered uniform Cartesian grid for the Eulerian fluid flow variables and a discrete set of points for the Lagrangian boundary variables. For a 2D case, the Eulerian grid nodes may be denoted as $\boldsymbol{x}_{ij}=(i\Delta x,j\Delta y)$ $(i=0,1,\cdots,n;j=0,1,\cdots,m)$, assuming the lower left corner of the domain is the origin. The Lagrangian grid points may be identified by $\boldsymbol{X}_k$ $(k=0,1,\cdots,n_b)$.

The interaction between variables defined at fluid nodes and variables defined at boundary grid points is governed by integration involving the Dirac delta function in the continuous equations (2.3) and (2.4). It may be numerically handled by introducing a regularized discrete delta function δ_h. The discretized form of Eqs. (2.3) and (2.4) using δ_h may be written as

$$\boldsymbol{f}_{ij}=\sum\nolimits_k \boldsymbol{F}_k\delta_h(\boldsymbol{x}_{ij}-\boldsymbol{X}_k)\Delta s_k,\tag{2.8}$$

$$\frac{\mathrm{d}\boldsymbol{X}_k}{\mathrm{d}t}=\boldsymbol{U}_k=\sum\nolimits_{i,j}\boldsymbol{u}_{ij}\delta_h(\boldsymbol{x}_{ij}-\boldsymbol{X}_k)\Delta x\Delta y,\tag{2.9}$$

where $\Delta x=\Delta y=h$ is the regular fluid grid spacing and Δs_k is the length of the kth boundary segment.

2.2 Discrete Dirac delta functions

The discrete delta function δ_h appearing in Eqs. (2.8) and (2.9) is a smoothed approximation to the Dirac delta function $\delta(\boldsymbol{r})$. The detailed derivations and specific forms were presented in literature [45, 51, 53]. The δ_h is normally expressed as

$$\delta_h(x,y)=\frac{1}{h^2}\phi\left(\frac{x}{h}\right)\phi\left(\frac{y}{h}\right),\tag{2.10}$$

where $\phi(r)$, with definition $r=\frac{x}{h}$, may take any of the following forms:

$$\phi_4^{\cos}(r)=\begin{cases}\frac{1}{4}\left[1+\cos\left(\frac{\pi r}{2}\right)\right], & |r|\leq 2,\\ 0, & |r|>2,\end{cases} \tag{2.11}$$

$$\phi_4^{\mathrm{IB}}(r)=\begin{cases}\frac{1}{8}\left(3-2|r|+\sqrt{1+4|r|-4r^2}\right), & 0\leq|r|<1,\\ \frac{1}{8}\left(5-2|r|-\sqrt{-7+12|r|-4r^2}\right), & 1\leq|r|<2,\\ 0, & |r|\geq 2.\end{cases} \tag{2.12}$$

$$\phi_5^{\mathrm{IB}}(r)=\begin{cases}\frac{17}{35}-\frac{1}{7}|r|^2+\sqrt{\frac{3123}{39200}-\frac{311}{980}|r|^2+\frac{101}{490}|r|^4+\frac{1}{28}|r|^6}, & 0\leq|r|<\frac{1}{2},\\ 1+\frac{1}{6}|r|-\frac{2}{3}|r|^2+\frac{1}{6}|r|^3-\frac{2}{3}\phi_5^{\mathrm{IB}}(|r|-1), & \frac{1}{2}\leq|r|<\frac{3}{2},\\ 1-\frac{19}{12}|r|+\frac{2}{3}|r|^2-\frac{1}{12}|r|^3+\frac{1}{6}\phi_5^{\mathrm{IB}}(|r|-2), & \frac{3}{2}\leq|r|<\frac{5}{2},\\ 0, & \frac{5}{2}\leq|r|.\end{cases} \tag{2.13}$$

$$\phi_6^{\mathrm{IB}}(r)=\begin{cases}\frac{61}{112}-\frac{11}{42}|r|-\frac{11}{56}|r|^2+\frac{1}{12}|r|^3+\frac{\sqrt{3}}{336}[243+1584|r| & \\ \quad -748|r|^2-1560|r|^3+500|r|^4+336|r|^5-112|r|^6]^{1/2}, & 0\leq|r|<1,\\ \frac{21}{16}+\frac{7}{12}|r|-\frac{7}{8}|r|^2+\frac{1}{6}|r|^3-\frac{3}{2}\phi_6^{\mathrm{IB}}(|r|-1), & 1\leq|r|<2,\\ \frac{9}{8}-\frac{23}{12}|r|+\frac{3}{4}|r|^2-\frac{1}{12}|r|^3+\frac{1}{2}\phi_6^{\mathrm{IB}}(|r|-2), & 2\leq|r|<3,\\ 0, & 3\leq|r|.\end{cases} \tag{2.14}$$

$$\phi_3^{\mathrm{IB}}(r)=\begin{cases}\frac{1}{3}\left(1+\sqrt{1-3|r|^2}\right), & 0\leq|r|<\frac{1}{2},\\ \frac{1}{6}\left(5-3|r|-\sqrt{-2+6|r|-3|r|^2}\right), & \frac{1}{2}\leq|r|<\frac{3}{2},\\ 0, & \frac{3}{2}\leq|r|,\end{cases} \tag{2.15}$$

$$\phi_4^{\mathrm{C}}(r)=\begin{cases}1-\frac{1}{2}|r|-|r|^2+\frac{1}{2}|r|^3, & 0\leq|r|<1,\\ 1-\frac{11}{6}|r|+|r|^2+\frac{1}{6}|r|^3, & 1\leq|r|<2,\\ 0, & 2\leq|r|,\end{cases} \tag{2.16}$$

$$\phi_2^{\mathrm{C}}(r)=\begin{cases}1-|r|, & |r|\leq 1,\\ 0, & |r|>1,\end{cases} \tag{2.17}$$

Graphs of these different forms of regularized discrete delta functions are shown in Fig. 1. Their different numerical features will be discussed later.

2.3 Lattice Boltzmann method for fluid flow

Defined on a regular lattice, the LB approach is very appropriate for the flow solver in the IB methods. In LB method, the flow is modeled as a group of fluid particles that are only allowed to move among lattice nodes or stay where they are. The composition of the lattice nodes depends on the chosen LB model. The most common lattice model for

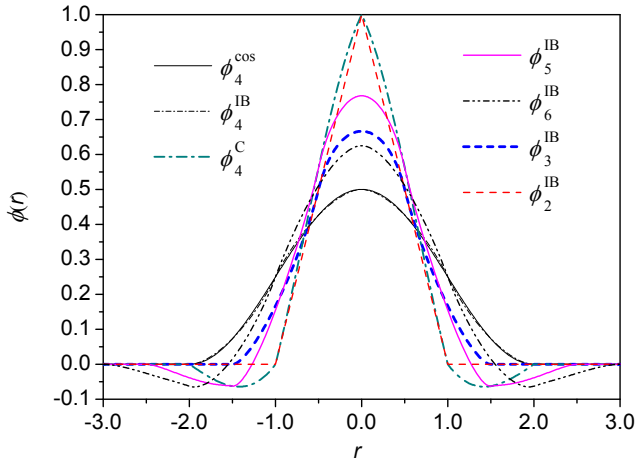

Figure 1: The profiles of the different regularized delta function $\phi(r)$'s.

two-dimensional simulations is the one using a square lattice with nine discrete velocity directions (denoted as D2Q9), while three-dimensional model normally uses a cubic lattice with fifteen discrete velocity directions (model D3Q15) [52].

The motion of fluid particles is governed by the discrete lattice Boltzmann equation. For problems with a body force, the common LB equation with Bhatnagar-Gross-Krook (BGK) collision operator is

$$f_\alpha(\boldsymbol{x}+\boldsymbol{e}_\alpha\Delta t,t+\Delta t)-f_\alpha(\boldsymbol{x},t)=-\frac{1}{\tau}[f_\alpha(\boldsymbol{x},t)-f_\alpha^{eq}(\boldsymbol{x},t)]+\Delta t g_\alpha(\boldsymbol{x},t), \tag{2.18}$$

where f_α is the particle velocity distribution function along the α-th particle velocity direction, f_α^{eq} the equilibrium distribution function, g_α the external forcing, τ the relaxation factor, $\boldsymbol{e}_\alpha$ the discrete particle vector, $\boldsymbol{x}$ the lattice grid, and Δt the time increment. The equilibrium distribution functions depending on variables ρ, $\boldsymbol{u}$ and $\boldsymbol{e}_\alpha$, are defined as [52]

$$f_\alpha^{eq}=w_\alpha\rho\left[1+3(\boldsymbol{e}_\alpha\cdot\boldsymbol{u})+\frac{9}{2}(\boldsymbol{e}_\alpha\cdot\boldsymbol{u})^2-\frac{3}{2}|\boldsymbol{u}|^2\right], \tag{2.19}$$

where the weighting parameters are w_α=4/9 as α=0, w_α=1/9 as α=1,2,3,4 and w_α=1/36 as α=5,6,7,8 for D2Q9 model, and w_α=2/9 as α=0, w_α=1/9 as α=1,2,$\cdots$,6 and w_α=1/72 as α=7,8,$\cdots$,14 for D3Q15 model in [52].

The macroscopic variables, namely the fluid density ρ and flow velocity $\boldsymbol{u}$, are defined in terms of the moments of the variable $f_\alpha(\boldsymbol{x},t)$ by

$$\rho(\boldsymbol{x},t)=\sum_\alpha f_\alpha(\boldsymbol{x},t),\quad \rho(\boldsymbol{x},t)\boldsymbol{u}(\boldsymbol{x},t)=\sum_\alpha \boldsymbol{e}_\alpha f_\alpha(\boldsymbol{x},t). \tag{2.20}$$

The above LB model is usually called the LBGK model. The simulation procedure is as follows: first, use (2.19) to calculate f_α^{eq}; secondly, evolve (2.18) to obtain f_α of the next

time step; thirdly, calculate ρ and $\boldsymbol{u}$ by (2.20); and finally insert ρ and $\boldsymbol{u}$ into (2.19) to get f_α^{eq} for the next time step.

Eq. (2.18) or its variant, along with $g_\alpha = 3w_\alpha \boldsymbol{f}\cdot\boldsymbol{e}_\alpha$, is widely used. It was applied in [34, 35, 37–39]. However, the treatment of the external forcing term by $\Delta t g_\alpha$ has only first-order accuracy because the external force $\boldsymbol{f}$ is in general unsteady in time and non-uniform in space. For problems of rigid or slowly moving boundaries or flexible boundary with small pressure gradient, the first-order method for the forcing term does not have any obvious effect on the global results. But for fast moving boundary and flexible boundary with large pressure gradient, higher order method is desirable. To improve the accuracy of treating external forcing term, Cheng presented a second-order scheme [40], where the LB equation is changed to

$$\begin{aligned} &f_\alpha(\boldsymbol{x}+\boldsymbol{e}_\alpha\Delta t,t+\Delta t)-f_\alpha(\boldsymbol{x},t)\\ =&-\frac{1}{\tau}[f_\alpha(\boldsymbol{x},t)-f_\alpha^{eq}(\boldsymbol{x},t)]+\frac{\Delta t}{2}[g_\alpha(\boldsymbol{x},t)+g_\alpha(\boldsymbol{x}+\boldsymbol{e}_\alpha\Delta t,t+\Delta t)], \end{aligned} \tag{2.21}$$

with the forcing term g_α being expressed as

$$g_\alpha = w_\alpha\{A+3\boldsymbol{B}\cdot[(\boldsymbol{e}_\alpha-\boldsymbol{u})+3(\boldsymbol{e}_\alpha\cdot\boldsymbol{u})\boldsymbol{e}_\alpha]\}, \tag{2.22}$$

in which A is the source term in the fluid continuity equation and $\boldsymbol{B}$ is the external forcing term for the momentum equation. For Eqs. (2.1) and (2.2), we can let $A=0$ and $\boldsymbol{B}=\boldsymbol{f}$.

The LBGK model using Eqs. (2.21) and (2.22) has a second-order accuracy in space for flows with unsteady and non-uniform forcing terms, which is consistent with the original LB model's accuracy. The second-order nature comes from the central-difference expression of the forcing term in (2.21) and the second-order term $(\boldsymbol{e}_\alpha\cdot\boldsymbol{u})\boldsymbol{e}_\alpha$ in (2.22). Because Eq. (2.21) is implicit (due to the term $g_\alpha(\boldsymbol{x}+\boldsymbol{e}_\alpha\Delta t,t+\Delta t)$), an iterative procedure should be used within each time step. Normally convergence can be reached within a few iterations.

2.4 IB-LBGK coupling procedure

In the IB-LBGK coupling scheme, we use the LBGK method to solve the fluid equations, namely the N-S equations (2.1) and (2.2), use the force formula (2.7) to calculate the boundary force, use the fluid node external force formula (2.8) to spread the boundary force to the fluid, and use formula (2.9) to interpolate the velocity of the boundary points from the velocities of the nearby fluid nodes. The exact procedure is depicted in Figure 3 of Ref. [43].

In every coupling cycle, an iteration process is needed because the scheme is semi-implicit. Indexed by m, the iteration ends when the convergence criterion is satisfied. Each iteration includes the following steps:

(1) Impose the fluid velocity on the boundary and update the position of boundary point to $\mathbf{X}_k^{n+1}$ by using formula (2.9);

(2) Calculate the force density $\mathbf{F}_k^{n+1}$ at the boundary points by using formula (2.7);

(3) Convert the boundary force $\mathbf{F}_k^{n+1}$ to the fluid external force $\mathbf{f}_{ij}^{n+1}$ by using formula (2.8);

(4) Calculate the LB method's external forcing terms $g_{\alpha,ij}^n$ and $g_{\alpha,ij}^{n+1}$ from fluid external forces $\mathbf{f}_{ij}^n$ and $\mathbf{f}_{ij}^{n+1}$ by using formula (2.22);

(5) Compute the LB equation (Eq. (2.21)) to obtain the distribution functions $f_{\alpha,ij}^{n+1}$;

(6) Calculate the fluid flow variables $\mathbf{u}_{ij}^{n+1}$ by formula (2.20);

(7) Conduct the similar steps of (1) and (2) to get the boundary force $\mathbf{F}_k^{n+1}$ for iteration cycle $m+1$.

(8) Compare the boundary force $\mathbf{F}_k^{n+1}$ at iteration step $m+1$ with that at iteration cycle m to check for the convergence.

If the convergence check is satisfied, then the calculation moves on to the next coupling cycle. This iteration is initially for obtaining a more accurate force introduction in the LB method. Fortunately, it brings in additional benefits for promoting stability. If the simulated problems are steady or slowly varying in time, and the stability is not a problem, the iteration cycle can be safely omitted.

3 Descriptions of the four testing cases

Four problems are chosen to verify the accuracy and stability of the IB-LBGK coupling scheme. The schematic illustrations of the problems are shown in Fig. 2. The relaxation of a circular membrane is mainly for analyzing the volume conservation and stability of the scheme. The shearing flow induced by a longitudinally moving fiber is for analyzing the near-boundary accuracy. The shearing flow near a rigid non-slip wall is mainly for analyzing the proper treatment of solid walls. And the circular Couette flow between two inversely rotating cylinders is for analyzing influence of grid alignment and orientation on the accuracy of the coupling method in the near-boundary regions.

3.1 Relaxation of a circular membrane

The relaxation of a circular elastic membrane to its equilibrium state is similar to the relaxation of a balloon, in which the inside fluid is conserved and there is a pressure jump between the inside and the outside. In Refs. [19, 29, 43, 45] the elliptic or flower-shaped membranes were studied, and vivid FSI and interesting flow patterns were shown. To simplify the problem, the circular membrane (Fig. 2(a)) is simulated here. It is a typical problem for testing the volume conservation and pressure maintenance. We assume that the relaxed radius (i.e. the radius of zero stress) of the circular membrane is $r_r = 0.4$, initially it is stretched to a circular shape of radius $r_i = 0.5$, and then is placed into a stationary fluid with uniform pressure p_i. Driven by the restoring force of the elastic boundary and the interaction of fluid inside and outside, the membrane relaxes with oscillations

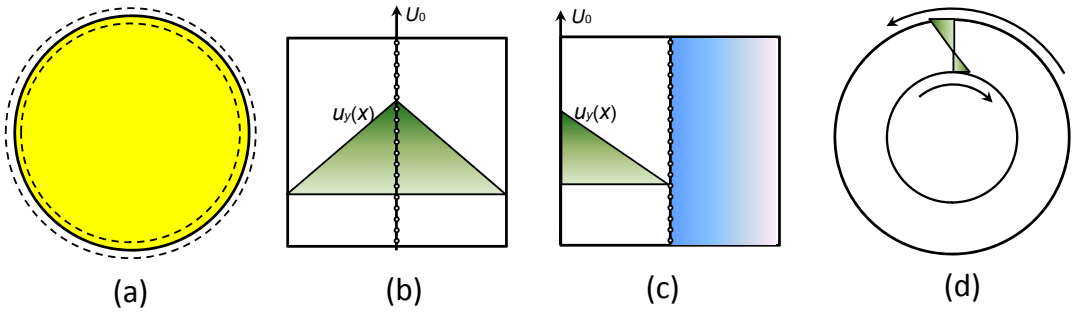

Figure 2: Schematic diagrams of the four cases. (a) The relaxation of a circular membrane; (b) the shearing flow induced by a longitudinally moving fiber; (c) the shearing flow near a non-slip rigid wall; (d) the circular Couette flow between two inversely rotating cylinders.

in pressure, velocity, fiber total length and enclosed fluid volume (area here), and finally settles down to an equilibrium circular steady state. The equilibrium circle radius r_e is slightly smaller than $r_i=0.5$ because the fluid simulated by the LB method is weakly compressible. If we use $\rho_0=1.0$ and $k_s=0.02$ and $\nu=0.001$, the radius of the equilibrium state should be $r_e=0.49307$, with an enclosed area $A_e=0.76377$ and inside-outside pressure jump Δp_e=9.438E-3. These theoretical values are obtained by MathCAD based on volume conservation, fluid compressibility and boundary elasticity. We simulate this FSI problem on a $[-1,1]\times[-1,1]$ domain, with the initial conditions $\boldsymbol{u}=\{u_x,u_y\}=\{0,0\}$ and $p=1/3$ on the whole flow field, and the boundary condition $p=1/3$ at the four sides. To record the history of flow variables, probe points $a(-0.5,0.0)$ and $c(0.0,0.0)$ are placed on the flow field, and points b and d are placed on the boundary, which are shown in Fig. 3. We first use $n\times m=N\times N=200\times 200$ lattice and $n_b=1200$ boundary grid-points to conduct simulations. To analyze parameter sensitivity, different values are also selected. We define $T=t/t_i$ as the normalized time, in which t is the time step that LB has simulated, and $t_i=d_i/u$ is the time that the fluid flows over a distance equivalent to the initial membrane diameter d_i.

3.2 Double-sided shearing flow induced by a moving fiber

The longitudinal movement of a straight fiber in the middle of a square flow domain can induce the double-sided shearing flow, as shown in Fig. 2(b). This case is typical because the velocity derivative across the fiber is discontinuous, which is common for FSI involving thin boundary structures such as filaments and sheets in flows [26, 32]. The fiber external force density is linearly distributed along the fiber length, for the velocity and shear stress are longitudinally uniform. Direct simulation of this flow is not convenient, because the fiber with finite length may move out of the domain and a periodic treatment is inappropriate due to the non-uniform fiber stretching force. Therefore, an equivalent flow field is simulated. The fiber is fixed in the middle of domain, the two side boundaries are set to move with velocity $U_y=0.1$, and the top and bottom flow

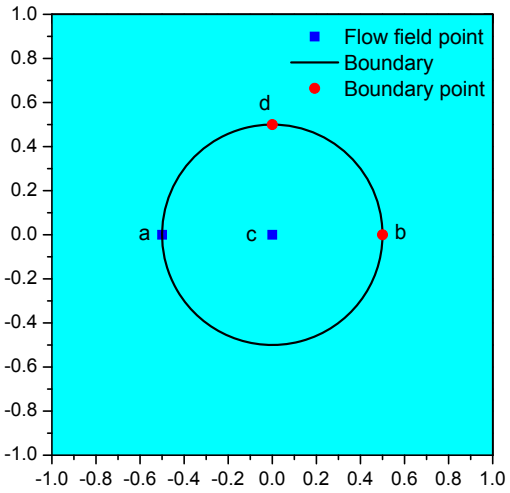

Figure 3: Probe points placed to show variable history for the relaxing membrane case. c is the center point of flow, a is the flow point corresponding to the left most point of the initial membrane, and b and d are the two boundary points.

boundaries are set to be periodic. $N\times N=100\times 100$ lattice is applied. A fiber of $n_b=400$ grid-points is stretched from $l_r=90$ to $l_i=100$ and placed vertically in the middle of the flow domain, then the two ends of the fiber coincide with the middle points of the upper and lower boundaries. The two ends of the fiber are fixed in the simulation. Fiber stiffness $k_s=2$, bending rigidity $k_b=2$ and fastening factor $k_f=2$ are used. When this flow field is subtracted from the uniform flow field $U_y=0.1$, the resultant flow is equivalent to the one induced by a moving fiber. The parameters mentioned above are used for the simulations, and the parameters will be adjusted in sensitivity analysis later.

3.3 Shearing flow near a non-slip rigid wall

The non-slip wall condition is a very common boundary condition in computational fluid dynamics. When using the IB-LB method to treat the moving boundary of a rigid solid object, such as a cylinder, fictitious flow patterns will appear inside the solid region [44]. The shearing flow near the non-slip wall (shown in Fig. 2(c)) is selected to verify whether the fictitious flow affects the accuracy of non-slip condition. We use similar conditions as the double-sided shearing flow: the fiber is fixed at the middle line and the velocity of the right side edge is zero.

3.4 Circular Couette flow

The above first case is for testing the volume conservation of the IB method via the coupling scheme. It is actually for testing the accuracy of normal velocity on the boundary, across which there exists a sharp pressure jump. The second and third cases are for testing

the accuracy of tangent velocity on the boundary, which is in alignment with the lattice edges. To test the accuracy of the method on a boundary that is not aligned with the lattice edges and bears both shear stress and pressure jump, a laminar circular Couette flow similar to the one in [46, 55] is selected.

The analytical solution of the laminar circular Couette may be expressed as [54]

$$u_\theta(r) = C_1 r + \frac{C_2}{r} \tag{3.1}$$

with factors

$$C_1 = \frac{(\Omega_2 R_2^2 - \Omega_1 R_1^2)}{(R_2^2 - R_1^2)}, \quad C_2 = \frac{(\Omega_1 - \Omega_2) R_1^2 R_2^2}{(R_2^2 - R_1^2)} \tag{3.2}$$

in which u_θ is the azimuthal velocity, r is the radius, Ω is the angular velocity of the cylinder, and R is the radius of the cylinder. The subscripts 1 and 2 are referred to the inner and outer cylinders, respectively.

When $R_1 = 40$, $R_2 = 60$, $\Omega_1 = -0.1/40$, and $\Omega_2 = 0.15/60$, the solutions $u_\theta(40) = -0.1$ and $u_\theta(60) = 0.15$ are obtained. These parameters are in the lattice unit. A special feature of this case as opposed to the circular Couette flows in the literature is that the two cylinders rotate in the opposite directions. Consequentially, severe shearing along the circular boundaries occurs which leads to a circular velocity inversion curve between the two cylinders, as demonstrated in Fig. 2(d).

The two cylinders, represented by $n_b = 551$ and $n_b = 826$ grid points, respectively, are placed at the center of a computational domain of $N \times N = 400 \times 400$ nodes, where the fixed pressure is imposed at the four sides.

The fastening position $\mathbf{Z}_k$ is updated at every time step to model the rotation of the two circular cylinders. Fiber stiffness $k_s = 1$, bending rigidity $k_b = 10$, and fastening factor $k_f = 20$.

4 Numerical analysis of the coupling scheme

4.1 Comparisons of different discrete delta functions

Ref. [53] presented the rules of building a regular discrete delta function, and gave two popular forms that are described in (2.11) and (2.12). Some other forms such as (2.13) and (2.17) are also applied in [45, 51]. Apart from different computing costs, different forms have different base stencils (i.e. interaction domain), which means different near boundary influence domain. The accuracy and stability are also different [33, 45, 51]. Which form of the above discrete delta function is the best for the IB-LBGK coupling? We try to answer this question in this section.

In the membrane relaxation case, the relative errors of the enclosed volume (area) and pressure are defined as $E_A = (A_e - A)/A_e$ and $E_P = (\Delta p_e - \Delta p_c)/\Delta p_e$, respectively. Here A is the membrane area and Δp_c is the pressure difference between the probe point c and the outside fluid.

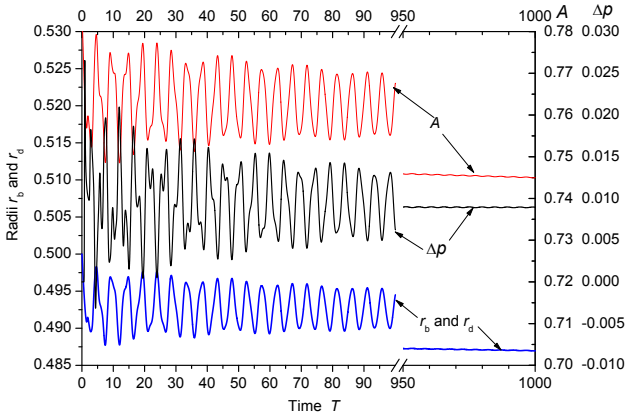

Figure 4: Histories of the enclosed area, pressure at center point c, and radius of the relaxing membrane. They are from the scheme with $\phi_4^{\rm IB}$ and 5 iterations per cycle, and the parameters are $N=200$, $n_b=1200$, $r_i=0.5$, $k_s=0.02$, $l_r=0.8l_i$, $\nu=0.001$.

Fig. 4 is the histories of the enclosed area, pressure at c, and radius of the relaxing membrane. They are from the scheme with discrete delta function $\phi_4^{\rm IB}$ and 5 iterations per cycle, and the parameters are $N=200$, $n_b=1200$, $r_i=0.5$, $k_s=0.02$, $l_r=0.8l_i$, $\nu=0.001$. We see that these quantities fluctuate obviously with large magnitudes in the early stage of relaxation, and the magnitudes attenuate gradually and finally converge to a near equilibrium state when the time is long enough. We compute A and Δp_c to evaluate the area leakage and pressure maintenance error at $T=1000$ (corresponding to 10^5 LB steps).

Fig. 5 is the wire-surface of pressure distribution at $T=1000$ by $\phi_4^{\rm IB}$ and 5-iteration

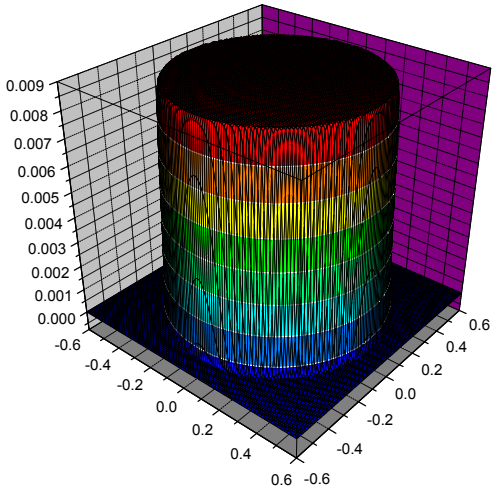

Figure 5: Wire-surface of the pressure value of the relaxing membrane at near equilibrium state $T=1000$. They are from the scheme with $\phi_4^{\rm IB}$ and 5 iterations per cycle, and the parameters are $N=200$, $n_b=1200$, $r_i=0.5$, $k_s=0.02$, $l_r=0.8l_i$, $\nu=0.001$.

per cycle. The inside pressure is well retained (the flat tableland) and the pressure jump on the border is very sharp with the bandwidth being only 4 grid points (counting the number of the wire-surface curves across the steep pressure jump region in Fig. 5), which is exactly the same as the base stencil of ϕ_4^{IB}.

Table 1 presents the relative errors by different discrete delta functions when the membrane relaxes to the equilibrium state at $T=1000$. It is clear that the scheme with the discrete delta functions $\phi_4^{\cos}$ and ϕ_4^{IB} have better volume conservation and pressure maintenance than others. These two forms have negligible differences and both of them result in $E_A<2.5\%$ and $E_P<5.5\%$. Given that the relaxing time is very long ($T=1000$), these results reveal a surprising accuracy of our coupling scheme for transversal flow across a boundary. ϕ_5^{IB} and ϕ_6^{IB} give poor results, even if they have wider base stencils. ϕ_3^{IB} also gives larger errors. We do not present the results of ϕ_4^{C} and ϕ_2^{C}, because simulations using them blow up at very early stage because of numerical instability.

Table 1: Volume leakage and pressure retention of different forms of the discrete Delta function. The membrane relaxation case at $T=1000$, with parameters $N=200$, $n_b=1200$, $r_i=0.5$, $k_s=0.02$, $l_r=0.8l_i$, $\nu=0.001$.

Parameters	Analytical	$\phi_4^{\cos}$	ϕ_4^{IB}	ϕ_5^{IB}	ϕ_6^{IB}	ϕ_3^{IB}
A	0.763773	0.744888	0.744984	0.620767	0.697842	0.692226
E_A		2.47%	2.46%	18.72%	8.63%	9.37%
Δp	0.009438	0.008933	0.008937	0.005023	0.007603	0.007447
E_P		5.35%	5.31%	46.77%	19.4%	21.1%

For the double-sided shearing flow case, the relative error of fiber force density is defined as $|F-F^*|/F^*$, where F^* is the analytical fiber force density and F is the mean force density over the middle reach of the $n_b/2$ grid-points (points numbered from $n_b/4$ to $3n_b/4$). The relative velocity error is defined as $E_u=\int|u_y(x)-u_y^*(x)|dx/\int u_y^*(x)dx$, where the $u_y^*(x)$ is the exact velocity and $u_y(x)$ is the computed velocity at the middle horizontal section of the channel.

Ref. [46] found velocity slip of the IB-LBGK coupling for this shearing flow and derived a formula for velocity slip. Here we also have the problem, and find that the errors are sensitive not only to the viscosity of the fluid but also to the discrete delta function used.

Fig. 6 shows the velocity profiles by different discrete delta functions at several typical viscosity values. The velocity slips at the fiber are obvious, the velocity profiles from different discrete delta functions are different, and the velocity deviation from the analytical velocity stems from the influence domain of the discrete delta function. For a given viscosity the velocity profiles differ from one another although they share similar patterns. For $\nu=0.1$ the profiles from ϕ_5^{IB} and ϕ_6^{IB} are closer to the analytical solution, but for $\nu\geq 0.5$ the profiles from $\phi_4^{\cos}$ and ϕ_4^{IB} are better. Fig. 7 and Table 2 present the relative errors of velocity and fiber force. The errors show similar patterns: for $\nu<0.5$ the errors are in the same range, and the differences from different delta functions are not as obvious as those from different values of viscosity; but for $\nu\geq 0.5$ the errors from $\phi_4^{\cos}$ and

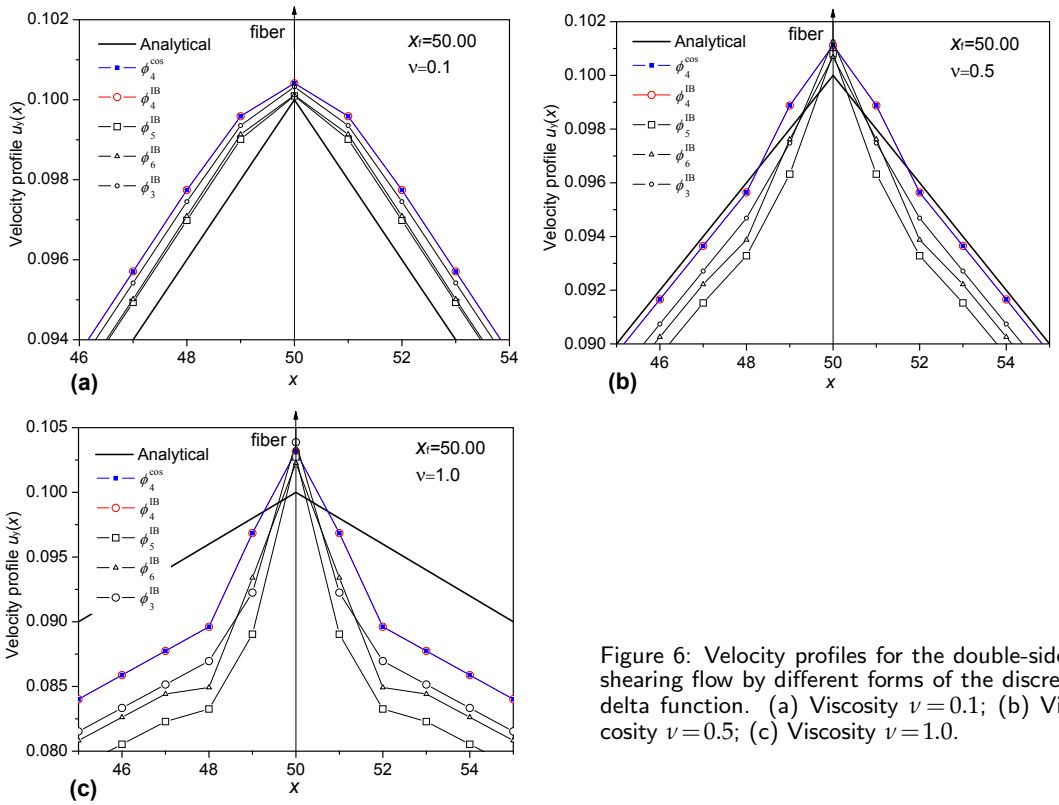

Figure 6: Velocity profiles for the double-sided shearing flow by different forms of the discrete delta function. (a) Viscosity $\nu=0.1$; (b) Viscosity $\nu=0.5$; (c) Viscosity $\nu=1.0$.

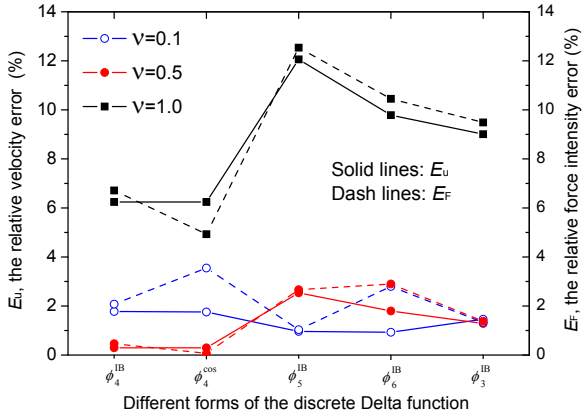

Figure 7: Relative velocity and force density errors for the double-sided shearing flow by different discrete delta functions.

ϕ_4^{IB} are the least compared to others. The effect of viscosity is more significant. Because of relatively smaller errors and moderate stencil size, the schemes with $\phi_4^{\cos}$ and ϕ_4^{IB} are recommended. Again, the simulations with ϕ_4^{C} and ϕ_2^{C} are unstable, and their results are not presented.

Table 2: Fiber force density errors for the double-sided shearing flow by different discrete delta functions,with simulation parameters $N=100$, $n_b=400$, $k_s=2.0$, $k_b=2.0$, $k_f=2.0$, $l_r=0.9l_i$.

Viscosity	Parameters	Analytical	$\phi_4^{\cos}$	ϕ_4^{IB}	ϕ_5^{IB}	ϕ_6^{IB}	ϕ_3^{IB}
0.1	F	4.000E-4	4.142E-4	4.083E-4	4.041E-4	3.888E-4	4.053E-4
	E_F		3.55%	2.08%	1.03%	2.80%	1.33%
0.5	F	0.002	0.00199	0.00200	0.001946	0.001942	0.001972
	E_F		0.46%	0.07%	2.67%	2.89%	1.39%
1.0	F	0.004	0.003731	0.00380	0.003498	0.00358	0.003621
	E_F		4.93%	6.71%	12.54%	10.45%	9.48%

To summarize, we have found that ϕ_5^{IB} and ϕ_6^{IB} have very poor accuracy in velocity and force and their near-boundary influence domains are relatively wider; ϕ_3^{IB}, although has a smaller influence domain, is also inferior in accuracy; ϕ_4^{C} and ϕ_2^{C} are poor for stability; $\phi_4^{\cos}$ and ϕ_4^{IB} are the most accurate with moderate near-boundary influence domains. Therefore, we recommend $\phi_4^{\cos}$ and ϕ_4^{IB}.

The remaining simulations and discussions are based on the use of ϕ_4^{IB}, unless otherwise stated.

4.2 Effect of iteration on the coupling procedure

Because the forcing term in (2.21) involves the influence of the next time step, strictly speaking, an implicit scheme is needed for advancing the LB equations. Here we introduce iterations in the coupling cycle at every time step where the LB equations are solved explicitly. However, when the time step of IB-LBGK coupling is far smaller than the characteristic time of the simulated problems, the iteration may be safely omitted. Theoretically, this omission just reduces the temporal accuracy of the forcing term from the second-order to the first-order, with no effect on the second-order accuracy in space. Practically, we find that the iteration procedure not only guarantees the second-order temporal accuracy but also improves the stability of simulations.

Fig. 8 shows the emergence of the instability at the early stage of the membrane relaxation. The red and black lines are the simulation results with 5 iterations and without iterations, respectively. The unstable phenomenon is obvious for the non-iteration case, and the stable and smooth curves are remained for the iterated case. At $T\approx 0.5$ the velocity $u_{x,a}$ begins to fluctuate irregularly, at $T\approx 0.8$ the enclosed area A begins to diverge (downward), and at $T\approx 1.4$ the pressure p_c begins to diverge (upward). Fig. 9 shows the unstable flow patterns at $T=1.0$ for the non-iteration simulation. It is clear that the unusual velocity vectors (represent velocities that soon blow up) first emerge from the boundary, which indicates the coupling scheme is the origin of numerical instability.

Fig. 10 shows the unstable flow patterns from the non-iteration coupling scheme for the circular Couette flow case. The smooth cylinders become zigzagged (the red lines).

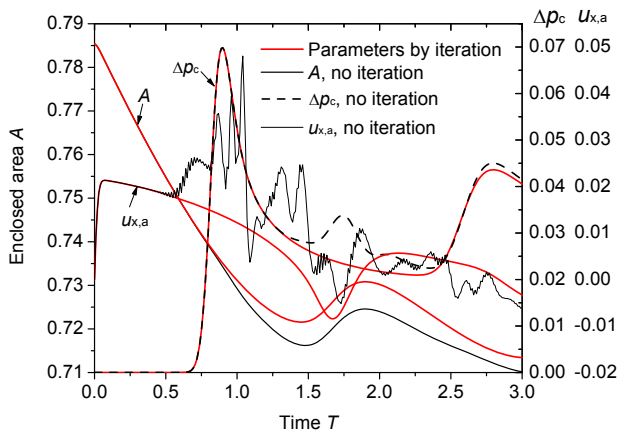

Figure 8: Stability comparison between the coupling schemes with and without iterations. The history of the enclosed area, pressure at center point c and x-velocity component at point a for the membrane relaxation case. $k_s=0.05$, $\nu=0.001$.

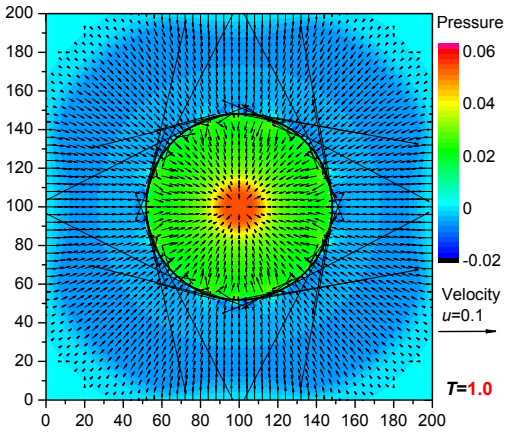

Figure 9: The unstable flow patterns at $T=1.0$, from the no-iteration coupling scheme for the membrane relaxation case. $k_s=0.05$, $\nu=0.001$.

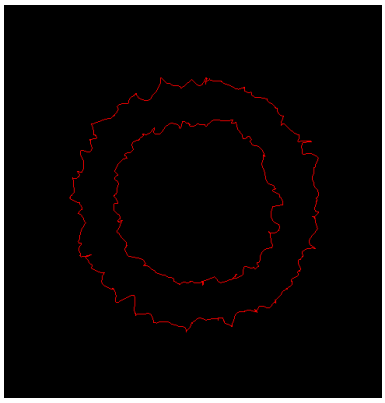

Figure 10: The unstable flow patterns from the no-iteration coupling scheme for the circular Couette flow case. The black background is resulted from the velocity vectors on the original white background. $k_s=1$, $k_b=10$ and $k_f=20$.

When iterations are applied, the strong boundary instability and noise in flow field have disappeared.

The instability of IB simulation is related to the stiffness of the boundary fibers. Rigid boundaries are more likely to become unstable in simulations. For the membrane relaxation case, the threshold of k_s that can be simulated stably by the 5-iteration scheme up to $T=1000$ is four times of that by the non-iteration scheme (see Table 3). Although not proportional to the number of iterations, the threshold of k_s is significantly increased. For the double-shearing flow and the circular Couette flow, if we use the non-iteration procedure, no stable results can be obtained. All reasonable results of these two cases are from 5-iteration scheme.

Table 3: Stability comparison between the coupling scheme with and without iterations. The thresholds of stiffness values that can be simulated stably up to $T=1000.0$ for the membrane relaxation case.

Viscosity	Maximum k_s from 5 iterations	Maximum k_s without iterations
0.1	0.20	0.05
0.5	0.40	0.10

The iteration scheme we introduce here does not substantially increase simulation cost, because it is actually a local update of the distribution functions within the interaction domain, not like the implicit scheme introduced in [41], where the equations involving all of the immersed boundary points have to be solved synchronously at every iteration.

We conclude that the iteration can greatly improve the robustness of the coupled IB-LBGK scheme without incurring substantial computing cost. This is the benefit of our semi-implicit scheme.

4.3 Importance of external forcing-term treatment

From the above subsection we know that the instability of the IB-LBGK coupling scheme is mainly caused by the boundary treatment, which is mainly affected by the forcing term treatment. Most of the previous works in the literature gave reasonable results by LB methods using the normal forcing term such as Eq. (2.18), which is adequate for problems involving open boundaries [41], rigid boundaries [34, 35, 37–39], and boundaries with small pressure jumps [30,31]. But this first-order approach is not enough for fast moving boundaries and boundaries of large pressure gradient. In these cases, methods of second-order accuracy for forcing-term treatment, i.e., those by Guo [49] and by Cheng [40], were applied [29,32,43,50]. What is the major difference among these methods?

In Ref. [43], it was pointed out that the LB methods with the normal forcing term gives negative volume leakage in the membrane relaxation case. This phenomenon suggests that the fluid flows into the membrane and the membrane will blow up eventually.

Fig. 11 is the enclosed-area history of using much smaller fiber stiffness $k_s=0.002$ that is only one tenth of the above simulations of the membrane relaxation. It is obvious that the volume using the normal forcing term $g_\alpha(\boldsymbol{x},t)$ (Eq. (2.18)) increases until it blows up near $T=32$. This is the evidence of a negative volume leakage. If we use the forcing term $g_\alpha(\boldsymbol{x}+\boldsymbol{e}_\alpha\Delta t,t+\Delta t)$, the volume will decrease with a positive leakage of nearly the same magnitude as the negative one from using the forcing term $g_\alpha(\boldsymbol{x},t)$. The new forcing term in Eq. (2.21) uses the average of $g_\alpha(\boldsymbol{x},t)$ and $g_\alpha(\boldsymbol{x}+\boldsymbol{e}_\alpha\Delta t,t+\Delta t)$, therefore, the volume leakage is nearly zero due to cancelation.

The forcing term proposed by Guo et al. [49] and used by Zhu [32] is actually a specific case of the new forcing term proposed by Cheng [40]. When the source term in the continuity equation is set to zero, Cheng's forcing term will be equivalent to Guo's forcing term, although their formulae are different. This has been verified by theoretical

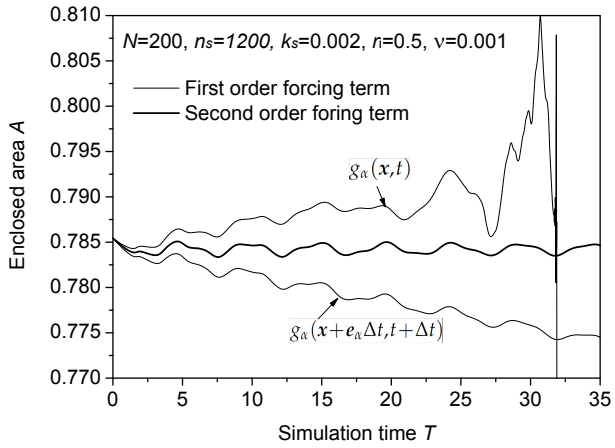

Figure 11: Comparison between the traditional forcing term and the new forcing term in the LB model. The volume histories are in the early stage of the membrane relaxation.

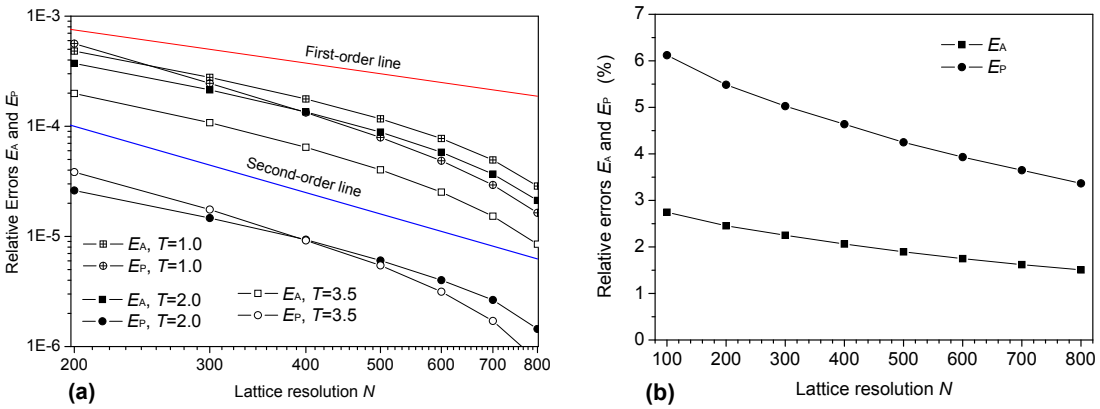

Figure 12: Convergence characteristics as the lattice resolution refines for the membrane relaxation case. (a) The convergence rates for parameters at several times in the early stage of membrane relaxation.(b) The dependence of errors on the lattice resolution as the membrane approaches equilibrium ($T=1000$).

derivation and numerical comparisons. Guo's forcing term is also semi-implicit because it needs the information at the next time-step in calculating $\boldsymbol{F}$. However, this fact was ignored by most users. For problems with slow temporal variations, neglecting the iteration does not produce significant errors.

Fig. 12(a) shows the spatial convergence characteristics at several typical time instants at early stage of the membrane relaxation. Because lack of analytical solutions, the numerical results on a fine lattice $N=800$ are set as the benchmark. The nearly second-order convergence is obvious (the faster convergence for $N>600$ is a side effect of the benchmark $N=800$, and should not be considered). At the near-equilibrium state $T=1000$, refinement also reduces the errors as shown in Fig. 12(b), but the precise order may not

be obtained. This is because the errors are comprehensive, including those due to temporal and spatial discretization, interaction algorithm, etc.

We conclude this section by stating that guaranteeing the second-order accuracy for the external forcing term in the IB-LBGK coupling scheme is crucial to numerical stability and overall accuracy. Both Cheng's and Guo's methods are good in practice. However, Cheng's method has clear physical interpretation and can be used when the source terms in the continuity equation also need to be considered.

4.4 Sensitivity to fluid/flow properties

4.4.1 Fluid viscosity

Viscosity is the fluid property that certainly affects numerical errors. Ref. [46] found the boundary slip is very sensitive to the viscosity of the fluid simulated by the LBGK. Presumably the leakage for problems like the membrane relaxation should decrease as viscosity becomes larger.

Fig. 13 shows that the errors at $T=1000$ for the membrane relaxation decrease sharply as the fluid viscosity increases ($\nu \leqslant 1.0$). After $\nu > 1.0$ the volume leakage and pressure loss decrease linearly with ν, and both are less than 2%.

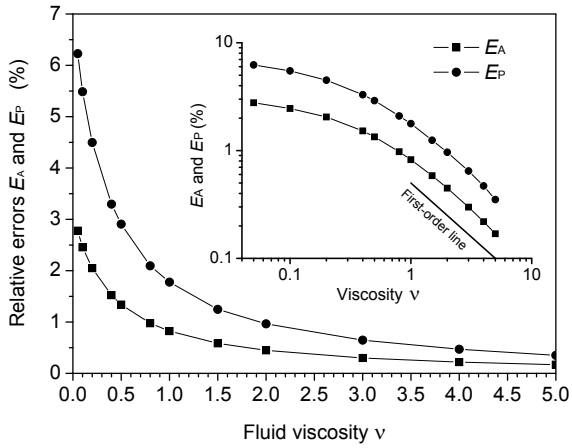

Figure 13: Error dependence on the fluid viscosity for the membrane relaxation case. Relaxed state $T=1000$.

Fig. 14 shows the velocity profile for the double-sided shearing flow. $x_f = 50$ means the fiber is located at the middle of the simulation domain ($N_X \times N_Y = 100 \times 100$). The velocity distributions within the stencil width are different for different viscosity, with $\nu \approx 0.5$ being the closest to the exact profile. This is consistent with the phenomenon in [46]. Fig. 15 shows the dependence of the error on the fluid viscosity for this case. The fiber force density F with $\nu \approx 0.4$ has the smallest error. Smaller viscosity $\nu < 0.4$ gives relative larger error but still within 5%. After $\nu > 1.0$ the error is proportional to

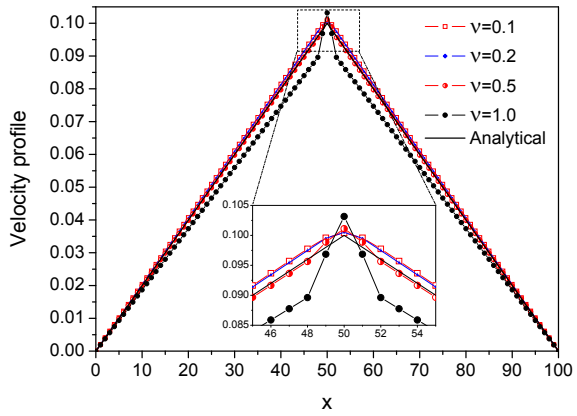

Figure 14: Velocity profiles of different fluid viscosity values for the double-side shearing flow case.

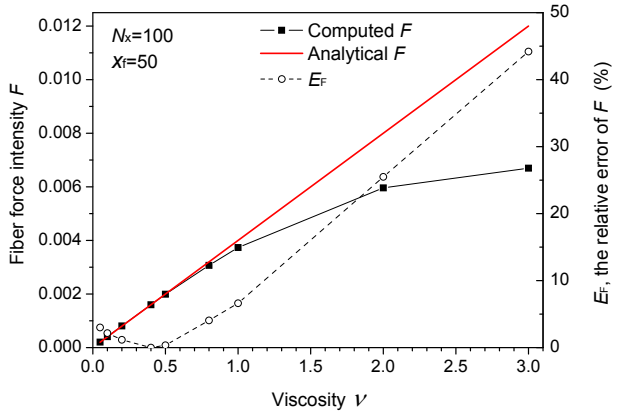

Figure 15: Error dependence on the fluid viscosity for the double-side shearing flow case.

the viscosity. The very large errors when $\nu > 1.0$ may be caused by large shearing force density.

The viscosity has different effects on the across-boundary error (boundary leakage) and the tangential boundary error (boundary slip). Increasing ν will incur smaller leakage, but may incur larger slip. For $\nu < 0.4$, both the leakage and slip errors increase slightly, but are within acceptable ranges. It is fortunate that the fluid viscosities in most IB-LB simulations are always small.

4.4.2 Shearing force density

Fig. 16 shows the velocity profiles of different shearing force densities (by varying channel widths) for the double-sided shearing flow case. Fig. 17 shows the dependence of error on the channel widths of this case. It is obvious that the errors increase as the shearing force density becomes larger. When $N_X > 40$ the error E_F does not decrease as N_X increases. To bound the errors of simulations the shearing force density should be

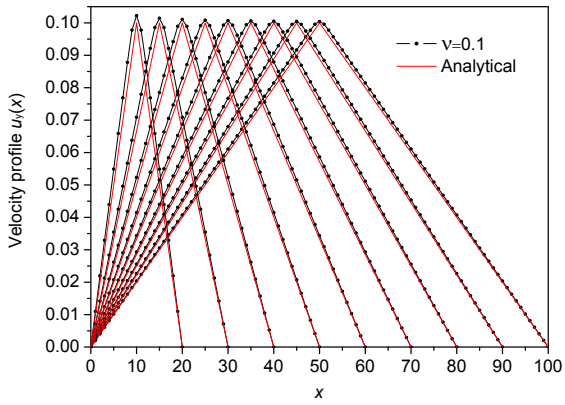

Figure 16: Velocity profiles of different shearing force intensities (by varying channel widths) for the double-side shearing flow case.

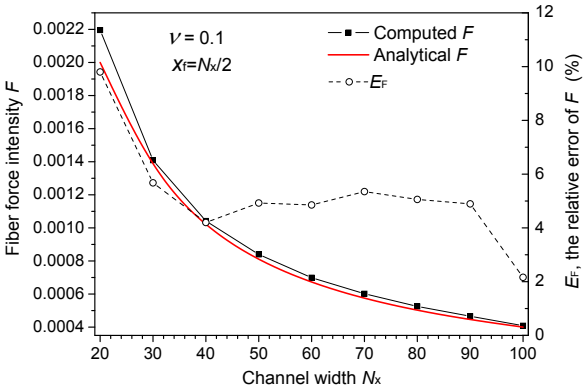

Figure 17: Error dependence on shearing force intensity for the double-side shearing flow case.

limited. But as the density decreases to a certain extent its influence on the errors may become negligible.

Fig. 18 shows the velocity profiles of non-symmetrical shearing forces (by varying the location of fiber, X_f) for the double-sided shearing flow case. Fig. 19 shows the dependence of the force error on the asymmetry. It is clear that as the degree of asymmetry of shearing becomes greater the errors become larger. The deviation of velocity profile is more serious in the weaker shearing side than in the stronger shearing side.

4.5 Sensitivity to boundary discretization parameters

4.5.1 Fiber segment length

Ref. [53] pointed out that $\Delta s \leq h/2$ is necessary to guarantee the non-slip boundary condition and to prevent fluid leakage across the boundary. But in practice, ensuring this condition anytime and anywhere is hard. It is desired to know the effect of Δs_k.

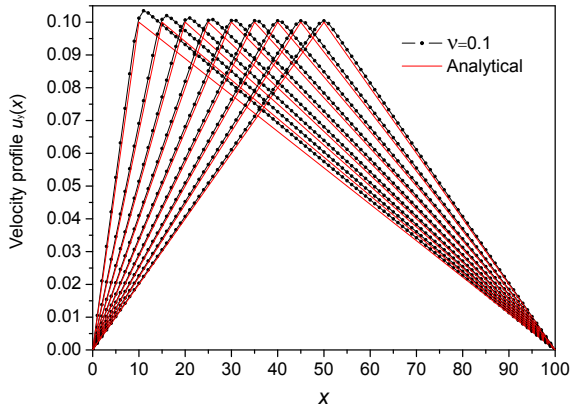

Figure 18: Velocity profiles of unsymmetrical shearing forces (by varying the location of fiber, X_f) for the double-side shearing flow case.

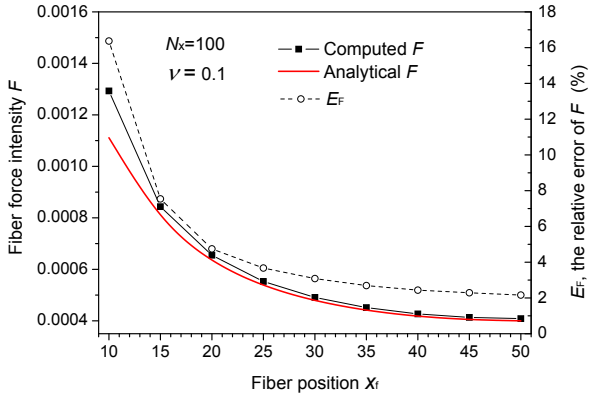

Figure 19: Error dependence on the unsymmetrical shearing forces for the double-side shearing flow case.

Fig. 20 shows the dependence of error on the fiber segment length for the membrane relaxation case. When $\Delta s < 1h$ the errors are very small, and the decrease of Δs has no obvious effects on errors; between $1h < \Delta s < 2h$, the errors increase slightly as Δs increases; when $\Delta s > 2h$ the errors increase significantly.

Fig. 21 shows the dependence of error on the fiber segment length for the double-sided shearing flow case. No obvious difference in errors is found in the range of $0.1h < \Delta s < 1h$.

The Δs varies constantly during a simulation. To get reasonable results $\Delta s < 2h$ must be guaranteed, and to get accurate results $\Delta s < 1h$ must be met.

4.5.2 Fiber orientation with respect to fluid grid

Boundary fiber segments are in general not in alignment with the fluid grid. Does this matter?

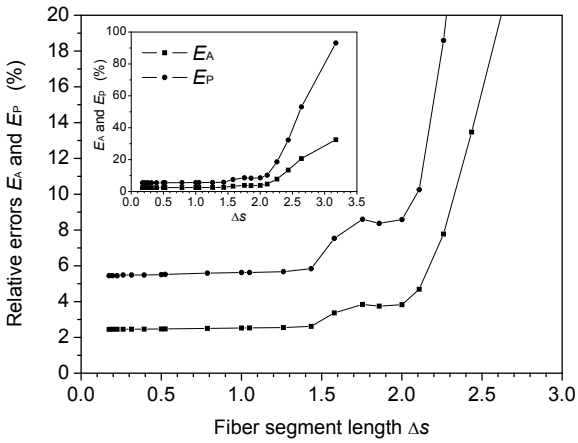

Figure 20: Error dependence on the fiber segment length for the membrane relaxation case.

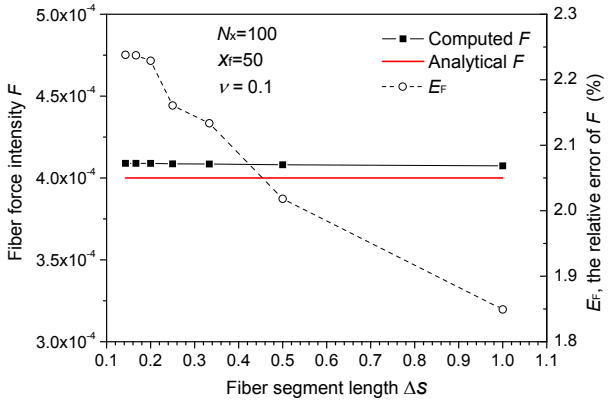

Figure 21: Error dependence on the fiber segment length for the double-side shearing flow case.

By placing the fiber in different location within the fluid domain, we investigate velocity profile of the double-sided shearing flow. Fig. 22 tells us that there is no obvious difference for the overall profile although the profile within the interaction region changes slightly.

Fig. 23 shows the magnitude distribution of the fluid flow force exerted by the boundaries of the rotating cylinders for the laminar circular Couette flow. The fluid flow force, shown in color splotch, are neither smooth nor axial symmetrical as would be in the ideal condition. The chessboard patterns in the four diagonal regions indicate that the force is sensitive to the alignment and orientation of the fiber. Fig. 24 shows the vectors of boundary force density along the cylinder boundaries. The force vectors on the outer cylinder are irregular in the four diagonal regions, and the vectors on the inner cylinder are disordered. These should be because the boundaries are not perpendicular or parallel to the fluid grid lines. Fig. 25 shows the azimuthal velocity error distribution. The patterns

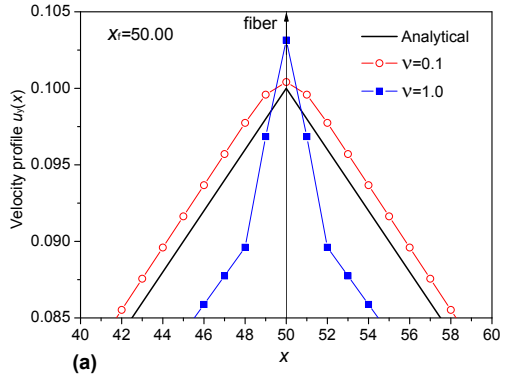

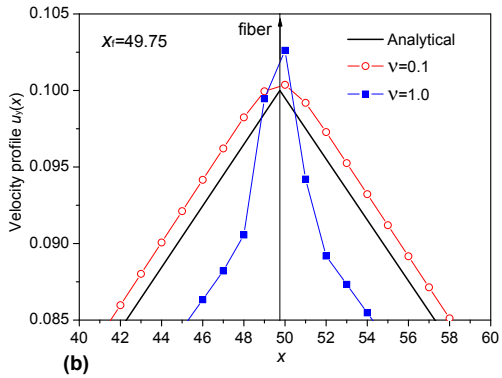

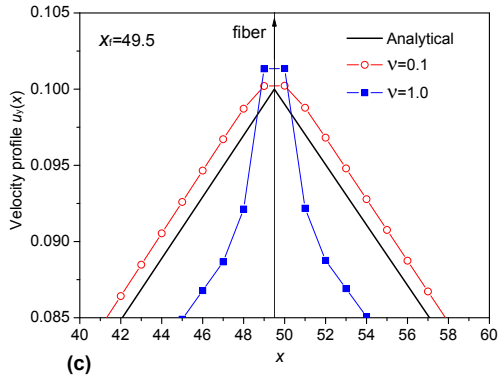

Figure 22: Velocity profiles as the fiber is located at different places with regards to fluid nodes for the double-side shearing flow case. (a)The fiber lies at fluid nodes. (b) The fiber lies of the nodes. (c) The fiber lies right in the middle of two fluid nodes.

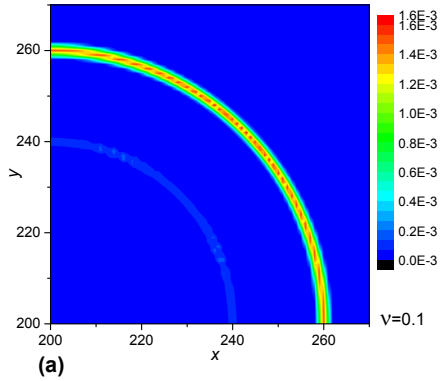

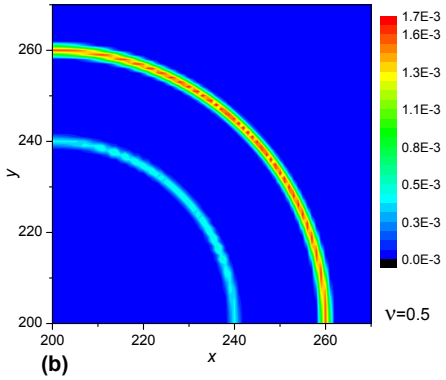

Figure 23: Fluid flow force distributions exerted by the boundaries of the rotating cylinders for the circular Couette flow case. The force value in the four diagonal regions are not uniform because the boundaries are not perpendicular or parallel to the grid lines. (a) $\nu=0.1$; (b)$\nu=0.5$.

for $\nu=0.1$ are the most axial symmetrical, but as ν becomes larger, they become position sensitive.

The asymmetric patterns indicate that the fiber orientation with the fluid grid has important effect on error distribution, especially when the boundary force is large. It is worth further investigation in the future.

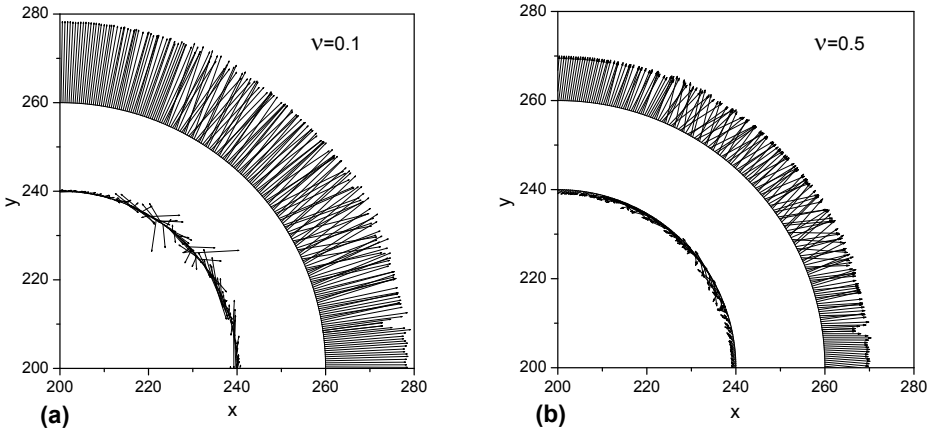

Figure 24: Vectors of the boundary force intensity along the rotating cylinders for the circular Couette flow case. The force vectors in the four diagonal regions are irregular because the boundaries are not perpendicular or parallel to the grid lines. The vectors on the inner cylinder are disorder. (a) $\nu=0.1$; (b)$\nu=0.5$.

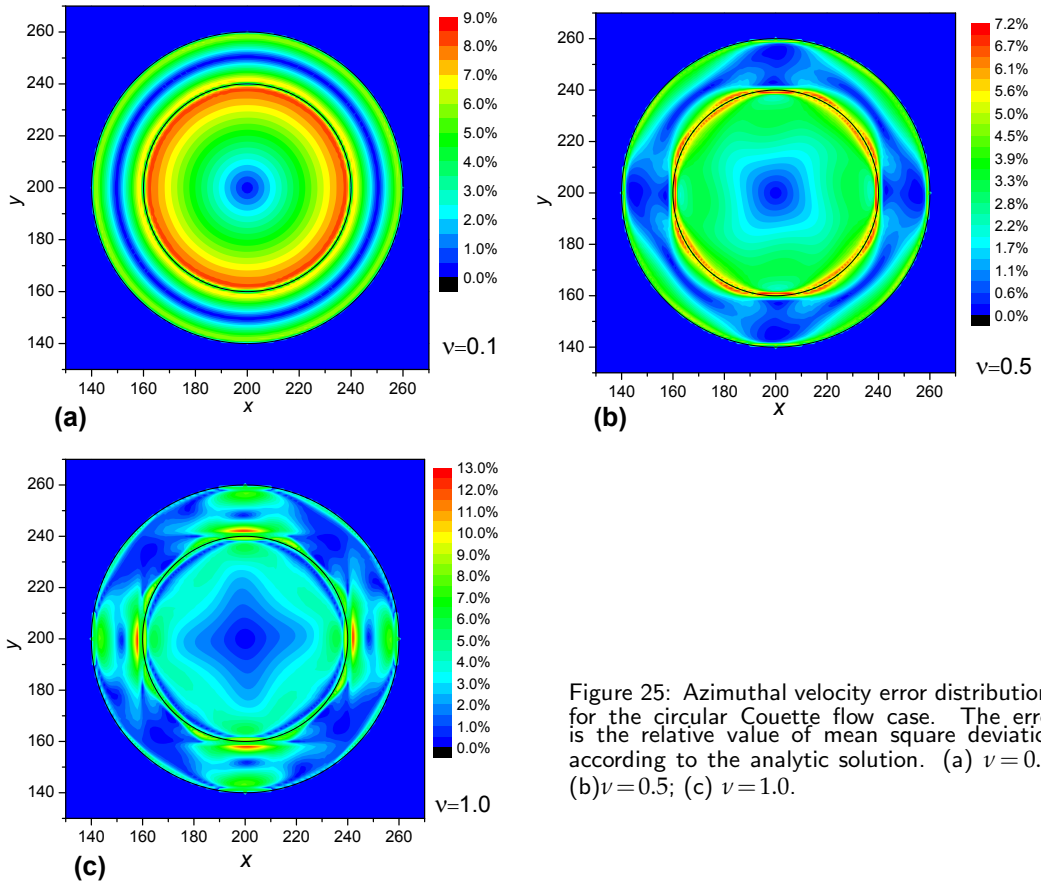

Figure 25: Azimuthal velocity error distributions for the circular Couette flow case. The error is the relative value of mean square deviation according to the analytic solution. (a) $\nu=0.1$; (b)$\nu=0.5$; (c) $\nu=1.0$.

4.6 Different treatments of the non-slip wall

In IB simulations, a solid boundary is treated by a set of discrete points connected by stiff virtual springs. These fibers (line segments connecting two neighboring points) endure one-sided shearing and normally induce fictitious flow on the other side, namely within the solid region.

Most works in the literature assumes the solid region as a fluid region, in which the flow velocity is used in the next time step [37, 53]. This may be termed as the method of flowing solid region. Another intuitive treatment is to re-initialize the solid region by zero velocity at every time step. It may be termed as the method of clear solid region. We use the one-sided shearing case to analyze which method is better.

The boundary slip phenomenon is similar to that of the double-shearing flow mentioned above, and the velocity profiles are also related to the viscosity of LBGK fluid, with $\nu \approx 0.5$ giving better approximation to the analytical solution (see Fig. 26). Fig. 27 is for investigating the accuracy of the two methods by comparing the relative velocity error E_u and relative shearing force error E_S (the shearing forces are derived from velocity gradients), which vary with different fluid viscosities. The errors are all the least around $\nu \approx 0.5$, at which the two methods have no discernible difference. When $\nu > 0.5$, the clear solid method gives smaller errors, but when $\nu < 0.5$, the flowing solid method gives smaller errors. When $\nu < 0.5$ the errors of the two methods both lie within an acceptable range, but the error with the flowing solid method is relatively smaller. Therefore, we suggest to use the flowing solid region method because one may choose smaller viscosity in most simulations.

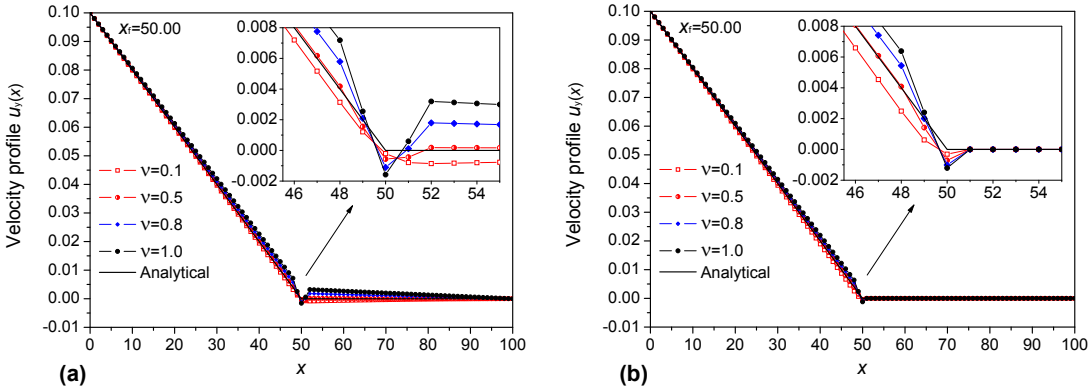

Figure 26: Velocity profiles of the near wall shearing flow. (a) By the flowing solid region method; (b) By the clear solid region method.

4.7 Clue of numerical instability

Numerical instability is a serious problem for the coupled IB-LBGK scheme. To improve the stability an implicit method [41] was proposed. And it was proven that the iteration

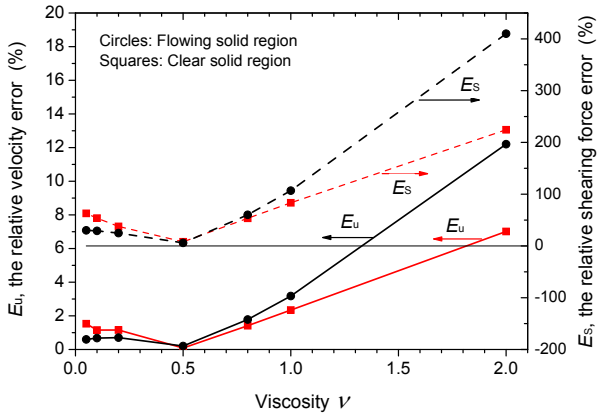

Figure 27: Error comparison between the two treatments of the solid region for the near wall shearing flow.

of the present scheme at every time step is beneficial to the improvement of numerical stability. From the above case studies we have found some clues of numerical instability, and these clues may help the future improvement of the coupled IB-LBGK scheme.

A large number of tests indicate that the emergence of both spatial and temporal high frequency fluctuations of fiber force or fiber segment length may be the initialization of the numerical instability. They are the precursors of the blow-up of simulations.

Fig. 28 shows history of the fluctuation of the fiber force for the membrane relaxation case. The history curve from the non-iteration coupling procedure begins to fluctuate after time step $t=40$, while the one by 5-iteration procedure gives a smooth curve. The simulation in the former case generates false physical quantities (although the values seem to be reasonable), will blow up after $t=300$. We see that the fluctuation has a cycle of 2 time-steps. Physical fluctuations are far slower than these numerical fluctuations.

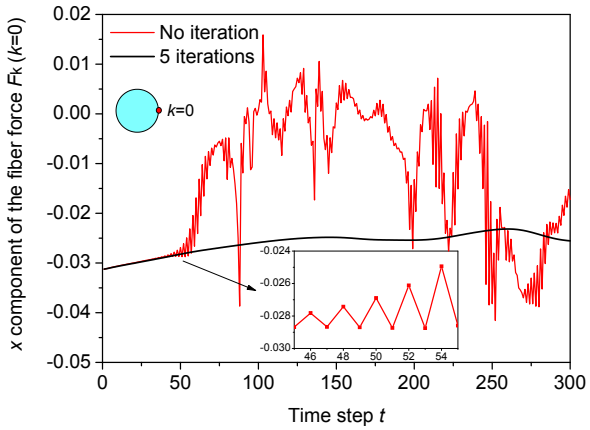

Figure 28: Fluctuating histories of the fiber force for the membrane relaxation case. The history curve from the no iteration coupling procedure is fluctuating, while the one by 5 iteration procedure is smooth.

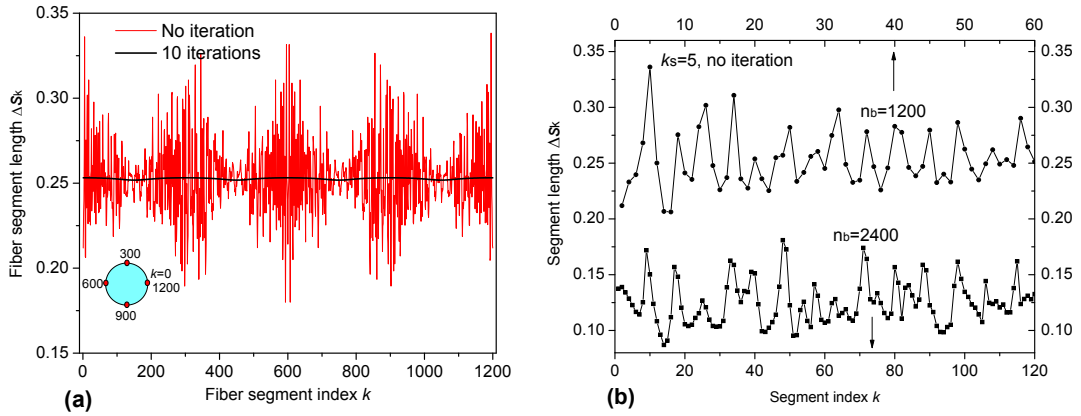

Figure 29: Spatial distributions of fiber segment lengths along the fiber for the membrane relaxation case at t=200. The lengths are location sensitive, and the wave lengths of fluctuation are all corresponding to 2 fluid grid spacings. (a) Along the whole fiber length as a circle with $n_b=1200$; (b) Local portrait of the fluctuating fiber segment lengths for $n_b=1200$ and $n_b=2400$.

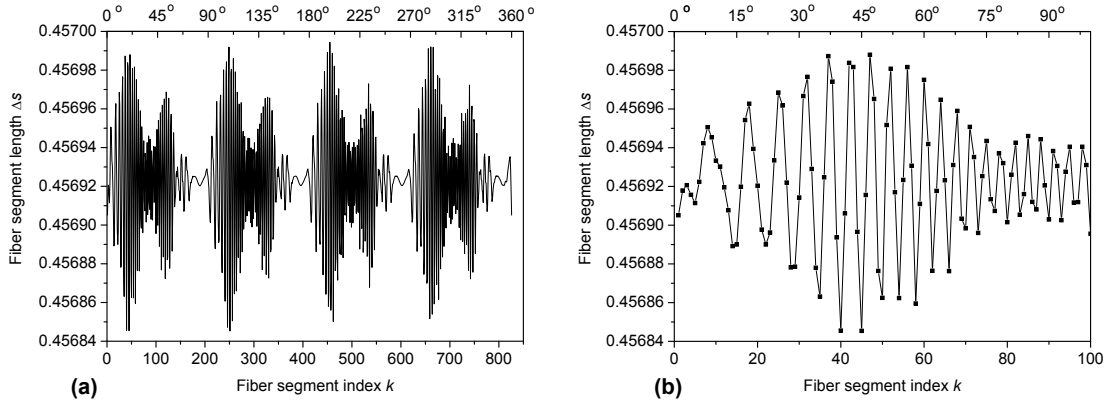

Figure 30: Fluctuations of the fiber segment lengths along the outer circle for circular Couette flow case at t=10000. (a) Along the whole fiber length as a 360° circle; (b) Local portrait of the fluctuating fiber segment lengths.

Fig. 29(a) shows the spatial fluctuation of fiber segment length at time step $t=200$ for the membrane relaxation case. The length is different at different position of the fiber, although they were set to be equal initially. The length fluctuations at the top, bottom, left, and right regions are more violent than in the four diagonal regions. This tells us again that the fiber orientation with respect to the fluid grid does matter. The length distribution curve with 10 iterations at every coupling cycle is very smooth, indicating that the iteration can damp the fluctuations effectively. Choosing different fiber segment numbers for the same problem, we have found that the wave length of the fluctuation is the same, approximately 2 fluid grid widths, as shown in Fig. 29(b).

Fig. 30 is the laminar circular Couette flow case. The fluctuation distribution of segment length reveals the same phenomenon as in Fig. 29. Again the fluctuation intensity

is related to the azimuth, and the fluctuation wavelength is approximately $2h$.

The instability may be detected by the emergence of high frequency sawtooth waves in the fiber force or the segment length, both in space and in time. And the cycle and wavelength, being two time-steps and two fluid grid-spacings, respectively, attest to the fact that the instability is caused by the treatment of the FSI interaction in the IB-LBGK scheme. Any measures that are able to damp the sawtooth fluctuations should be tried to improve the stability of the coupling scheme.

5 Conclusions

Based on the technique details reported above, some conclusions may be drawn as follows. The first discrete delta function (cosine function) used in the IB methods is almost equivalent to the late introduced piecewise approximation ϕ_4^{IB}, and both have better accuracy than others for our IB-LBGK coupling. The iteration in the coupling scheme can effectively improve numerical stability. The treatment of the external forcing term in the IB-LBGK method is crucial for both accuracy and robustness, and a second-order approach for the forcing term should be applied. Fluid and flow properties such as viscosity and flow gradients, boundary discretization parameters such as discrete fiber segment length, and boundary orientations all have substantial effects on accuracy and stability of the coupling scheme. The emergence of fluctuations of the boundary and the nearby flow field in both time and space appears to be the origination of the numerical instability associated with the coupling scheme. These detailed results may offer hints for effective usage and future improvement of the IB-LBGK coupling method for fluid-structure interactions.

Acknowledgments

This work was supported by the National Natural Science Foundation of China (NSFC, Grant numbers 10572106, 10872153 and 11172219) and the Specialized Research Fund for the Doctoral Program of Higher Education of China (Grant No. 20130141110013).

References

[1] C.S. Peskin, Flow patterns around heart valves: a digital computer method for solving the equations of motion, PhD thesis, Physiol., Albert Einstein Coll. Med., Univ. Microfilms, 378 (1972), 72-102.

[2] C.S. Peskin and D.M. McQueen, A general method for the computer simulation of biological systems interacting with fluids-Biological fluid dynamics, Ellington C. P. et al. (Ed.), The company of biologists limited, Cambridge, 1995.

[3] D.M. McQueen and C.S. Peskin, A three-dimensional computer model of the human heart for studying cardiac fluid dynamics, Computer Graphics, 34 (2000), 56-60.

[4] J.D. Lemmon and A.P. Yoganathan, Three-dimensional computational model of left heart diastolic function with fluid-structure interaction, J. Biomech. Eng., 122 (2000), 109-117.
[5] D.M. McQueen, C.S. Peskin, and E.L. Yellin, Fluid dynamics of the mitral valve: physiological aspects of a mathematical model, Am. J. of Physiol., 242 (1982), 1095-1110.
[6] B.E. Griffith, X. Luo, D.M. McQueen, and C.S. Peskin, Simulating the fluid dynamics of natural and prosthetic heart valves using the immersed boundary method, Int. J. App. Mech., 1(1) (2009), 137-177.
[7] L. Fauci and C.S. Peskin, A computational model of aquatic animal locomotion, J.Comput. Phys., 77 (1988), 85-108.
[8] E. Givelberg, Modeling elastic shells immersed in fluid, PhD thesis, Courant Institute of Mathematical Sciences, New York University, September (1997).
[9] N.T. Wang and A.L. Fogelson, Computational methods for continuum models of platelet aggregation, J. Comput. Phys., 151 (1999), 649-675.
[10] D. Sulsky and J.U. Brackbill, A numerical method for suspension flow, J. Comput. Phys. 96(1991):339-368.
[11] E. Jung and C.S. Peskin, 2-D simulation of valveless pumping using the immersed boundary method, SIAM J. Sci. Comput., 23(1) (2001), 19-45.
[12] K.M. Arthurs, L.C. Moore, C.S. Peskin et al., Modeling arteriolar flow and mass transport using the immersed boundary method, J. Comput. Phys., 147 (1998), 402-440.
[13] D.C. Bottino, Modeling viscoelastic networks and cell deformation in the context of the immersed boundary method, J. Comput. Phys., 147 (1998), 86-113.
[14] L.A. Miller and C.S. Peskin, Flexible fling in tiny insect flight, J. Exp. Biol., 212(19) (2009), 3076-3090.
[15] Y. Kim, S. Lim, S.V. Raman et al., Blood flow in a compliant vessel by the immersed boundary method, Ann. Biomed. Eng., 37(5) (2009), 927-942.
[16] J. Teran, L.J. Fauci, and M. Shelley, Viscoelastic fluid response can increase the speed and efficiency of a free swimmer, Phys. Rev. Lett., 104 (2010), 038101.
[17] A. Naji, P.J. Atzberger, and F.L. Brown, Hybrid elastic and discrete-Particle approach to biomembrane dynamics with application to the mobility of curved integral membrane proteins, Phys. Rev. Lett., 102(13) (2009), 138102.
[18] Y. Kim and C.S. Peskin, 2-D parachute simulation by the immersed boundary method, SIAM J. Sci. Comput., 28(6) (2006), 2294-2312.
[19] Z.L. Li and M.C. Lai, Immersed interface methods for Navier-Stokes equations with singular forces, J. Comput. Phys., 171 (2001), 822-842.
[20] R. Cortez and M. Minion, The blob projection method for immersed boundary problems, J. Comput. Phy., 161 (2000), 428-453.
[21] X.S. Wang, From immersed boundary method to immersed continuum method, Int. J. Multiscale Compu. Eng., 4(1) (2006), 127-145.
[22] W.K. Liu, D.K. Kim, and S. Tang, Mathematical foundations of the immersed finite element method, Computational Mechanics, 39(3) (2007), 211-222.
[23] C.S. Peskin and B.F. Printz, Improved volume conservation in the computation of flows with immersed elastic boundaries, J. Comp. Phys., 105 (1993), 33-49.
[24] B.E. Griffith, R.D. Hornung, D.M. McQueen, and C.S. Peskin, An adaptive, formally second order accurate version of the immersed boundary method, J. Comput. Phys., 223(1) (2007), 10-49.
[25] M.C. Lai and C.S. Peskin, An immersed boundary method with formal second order accuracy and reduced numerical viscosity, J. Comput. Phys., 160 (2000), 705-719.

[26] L. Zhu and C.S. Peskin, Simulation of a flexible flapping filament in a flowing soap film by the immersed boundary method, J. Comput. Phys., 179(2) (2002), 452-468.
[27] Y. Kim and C.S. Peskin, Penalty immersed boundary method for an elastic boundary with mass, Phys. of Fluids, 19(5) (2007), 053103.
[28] T.Y. Hou and Z. Shi, An efficient semi-implicit immersed boundary method for the Navier-Stokes equations, J. Comput. Phys., 227 (2008), 8968-8991.
[29] Y.G. Cheng and H. Zhang, Immersed boundary method and lattice Boltzmann method coupled FSI simulation of mitral leaflet flow, Comput. & Fluids, 39(5) (2010), 871-881.
[30] J. Zhang, P.C. Johnson, and A.S. Popel, An immersed boundary lattice Boltzmann approach to simulate deformable liquid capsules and its application to microscopic blood flows, Phys. Biol., 4 (2007), 285-295.
[31] J. Zhang, P.C. Johnson, and A.S. Popel, Red blood cell aggregation and dissociation in shear flows simulated by lattice Boltzmann method, J. Biomech., 41 (2008), 47-55.
[32] L. Zhu, G. He, S. Wang et al., An immersed boundary method based on the lattice Boltzmann approach in three dimensions, with application, Comput. & Math. with Applications, 61 (2011), 3506-3518.
[33] T. Krueger, F. Varnik, and D. Raabe, Efficient and accurate simulations of deformable particles immersed in a fluid using a combined immersed boundary lattice Boltzmann finite element method, Comput. & Math. with Applications, 61 (2011), 3485-3505.
[34] Z.G. Feng and E.E. Michaelides, The immersed boundary-lattice Boltzmann method for solving fluid-particles interaction problems, J. Comput. Phys., 195 (2004), 602-628.
[35] Y. Peng, C. Shu et al., Application of multi-block approach in the immersed boundary-lattice Boltzmann method for viscous fluid flows, J. Comput. Phys., 218 (2006), 460-478.
[36] Y. Peng and L.-S. Luo, A comparative study of immersed-boundary and interpolated bounce-back methods in LBE, Progress in Comput. Fluid Dyn., 8(1-4) (2008), 156-166.
[37] C. Shu, N. Liu and Y.T. Chew, A novel immersed boundary velocity correction-lattice Boltzmann method and its application to simulate flow past a circular cylinder, J. Comput. Phys., 226 (2007), 1607-1622.
[38] A. Dupuis, P. Chatelain, and P. Koumoutsakos, An immersed boundary-lattice Boltzmann method for the simulation of the flow past an impulsively started cylinder, J. Comput. Phys., 227 (2008), 4486-4498.
[39] X.D. Niu, C. Shu, Y.T. Chew, and Y. Peng, A momentum exchange-based immersed boundary-lattice Boltzmann method for simulating incompressible viscous flows, Phys. Lett. A, 354 (2006), 173-182.
[40] Y.G. Cheng and J.P. Li, Introducing unsteady non-uniform source terms into the lattice Boltzmann model, Int. J. Num. Meth. Fluids, 56 (2008), 629-641.
[41] J. Hao and L. Zhu, A lattice Boltzmann based implicit immersed boundary method for fluid-structure-interaction, Computers and Mathematics with Applications, 59 (2010), 185-193.
[42] F.B. Tian, H. Luo, L. Zhu et al., An efficient immersed boundary-lattice Boltzmann method for the hydrodynamic interaction of elastic filaments, J. Comput. Phys., 230(19) (2011), 7266-7283.
[43] Y.G. Cheng, H. Zhang, and C. Liu, Immersed Boundary-Lattice Boltzmann Coupling Scheme for Fluid-Structure Interaction with Flexible Boundary, Commun. Comput. Phys., 9(5) (2011), 1375-1396.
[44] S.K. Kang and Y.A. Hassan, A comparative study of direct-forcing immersed boundary-lattice Boltzmann methods for stationary complex boundaries, Int. J. Num. Meth. Fluids,

66(9) (2011), 629-641.
[45] B.E. Griffith and C.S. Peskin, On the order of accuracy of the immersed boundary method: Higher order convergence rates for sufficiently smooth problems, J. Comput. Phys., 208 (2005), 75-105.
[46] G. Le and J. Zhang, Boundary slip from the immersed boundary lattice Boltzmann models, Phys. Rev. E, 79(2) (2009), 026701.
[47] E.P. Newren, Enhancing the immersed boundary method: stability, volume conservation and implicit solvers, PhD dissertation of the University of Utah, USA, 2007.
[48] E.P. Newren, A.L. Fogelson, R.D. Guy, and R.M. Kirby, Unconditionally stable discretizations of the immersed boundary equations, J. Comput. Phys., 222 (2007), 702-719.
[49] Z. Guo, C. Zheng and B. Shi, Discrete lattice effects on the forcing term in the lattice Boltzmann method, Phys. Rev. E, 65(4) (2002), 046308.
[50] J. Wu and C. Shu, Implicit velocity correction-based immersed boundary-lattice Boltzmann method and its applications, J. Compu. Phys., 228 (2009), 1963-1979.
[51] T.T. Bringley, Analysis of the immersed boundary method for Stokes flow, PhD dissertation, New York University, 2008.
[52] S. Chen and G.D. Doolen, Lattice Boltzmann method for fluid flows, Annu. Rev. Fluid Mech., 30 (1998), 329-364.
[53] C.S. Peskin, The immersed boundary method, Acta Numerica, 11 (2002), 479-517.
[54] C. Pozrikidis, Introduction to Theoretical and Computational Fluid Dynamics, Oxford University Press, Oxford, New York, 1997.
[55] S. Xu, Z.J. Wang, An immersed interface method for simulating the interaction of a fluid with moving boundaries, J. Comput. Phys., 216 (2006), 454-493.